

THE ASCA X-RAY SPECTRUM OF ARP 102B AND EVALUATION OF SIMPLE MODELS FOR ITS ASSOCIATED, METASTABLE FE II ABSORBER

MICHAEL ERACLEOUS¹, JULES P. HALPERN², & JANE C. CHARLTON¹
Draft version October 27, 2018

ABSTRACT

We have observed the broad-line radio galaxy Arp 102B with *ASCA* in order to determine the absorbing column density towards its X-ray source and measure its X-ray spectrum. The ultimate goal was to constrain the properties of the medium responsible for the metastable Fe II absorption lines observed in the ultraviolet spectrum of this object. The 0.5–10 keV X-ray spectrum is best described by a simple power-law model of photon index 1.58 ± 0.04 modified by photoelectric absorption with an equivalent hydrogen column density of $(2.8 \pm 0.3) \times 10^{21} \text{ cm}^{-2}$. An Fe K α line is not detected with an upper limit to its equivalent width of 200 eV, assuming that its full width at half maximum is 60,000 km s⁻¹. Using the column density measured from the X-ray spectrum and the observed spectral energy distribution as constraints, we explore simple (single-zone, constant-density) photoionization models for the absorber for a wide range of densities and ionization parameters in an effort to reproduce the strengths of the ultraviolet absorption lines. We find that densities of at least 10^{11} cm^{-3} are needed. However, a single ionization parameter cannot explain all of the observed lines. An ionization parameter between $10^{-2.5}$ and $10^{-3.5}$ is needed to explain the Mg and Fe lines and the soft X-ray absorption, but the observed lines (from Si, C, Al, and H) require different density–ionization parameter combinations. According to the models, such an absorbing medium must be located very close to the source of ionizing radiation (within 5,000 gravitational radii) and must be very compact. As such, the properties of this absorbing medium differ from those of more luminous quasars, but are reminiscent of the absorber in the Seyfert galaxy NGC 4151. We suggest that the absorber is in the form of thin sheets or filaments embedded in an outflowing wind that overlays the accretion disk of Arp 102B. This picture is consistent with all of the available constraints on the central engine of this object. In an appendix, we present the X-ray spectrum of the source MS 1718.6+4902, which happened to fall within the field of view of the *ROSAT* PSPC and the *ASCA* GIS during the observations of Arp 102B.

Subject headings: galaxies: active—galaxies:individual (Arp 102B, MS 1718.6+4902)— X-rays: galaxies—line: formation

1. INTRODUCTION

The broad-line radio galaxy (BLRG) Arp 102B (Stauffer, Schild, & Keel 1983; Chen, Halpern, & Filippenko 1989; Chen & Halpern 1989) is the prototype of a subset of radio-loud active galactic nuclei (AGNs) with double-peaked Balmer lines in their optical spectra (see more examples in Eracleous & Halpern 1994). The profiles of these double-peaked emission lines and a number of additional, extreme spectroscopic properties of these objects have led to the interpretation that they harbor line emitting accretion disks whose inner parts have the form of an optically thin, geometrically thick ion torus (Chen & Halpern 1989; Eracleous & Halpern 1994). The ion torus (Rees et al. 1982) is very similar to what is known today as an advection-dominated accretion flow (ADAF; Narayan & Yi 1994, 1995), a structure which is realizable at accretion rates considerably lower than the Eddington rate. Although alternative scenarios for the origin of the double-peaked lines have been proposed, these are disfavored by the observational evidence available today (see reviews by Eracleous 1998, 1999).

In the process of studying the UV spectroscopic properties of AGNs with double-peaked emission lines we obtained a spectrum of Arp 102B with the *Hubble Space*

Telescope (HST), which revealed an unexpected complex of Fe II *absorption* lines very close to its systemic redshift (Halpern et al. 1996). This complex includes much more than the transitions from the ground state of Fe II that are often observed in quasar absorption line systems and the interstellar medium (multiplets UV1, UV2, and UV3 from the a^6D ground state term): it also includes multiplets from the next two lowest states (terms a^4F and a^4D). Particularly surprising is the presence of multiplets UV62, UV63, and UV64, arising from the metastable a^4D term, which lies 0.99–1.10 eV above the ground state. Since absorption from excited states of Fe II is incompatible with the diffuse interstellar medium of the host galaxy and with intervening absorption-line systems, the absorber is most likely intrinsic to Arp 102B and its association with the active nucleus remains to be understood. Metastable Fe II absorption lines are not observed in Seyfert galaxies very often, with NGC 4151 being one of the rare examples (Kraemer et al. 2001). NGC 4151 also shows a C III] $\lambda 1176$ line, arising from a level 6.05 eV above the ground state (Kriss et al. 1995). Absorption lines from the ground state of Fe II have been observed in some other Seyfert galaxies, for example, NGC 3227 (Crenshaw et al. 2001). In marked contrast with Seyfert galaxies, Fe II absorption

¹ Department of Astronomy and Astrophysics, The Pennsylvania State University, 525 Davey Lab, University Park, PA 16802

² Department of Astronomy Columbia University, 538 West 120th Street, New York, NY 10027

lines from metastable states are often seen in the spectra of quasars. Examples that have been known for quite some time include Q 0059–2735 (Hazard et al. 1987; Wampler, Chugai, & Petitjean 1995), Hawaii 167 (Cowie et al. 1994), and Mrk 231 (Boroson, Meyers, & Morris 1991; Smith et al. 1995). Recently, a number radio-loud quasars from the FIRST radio survey (Becker, White, & Helfand 1995) have been found to host metastable Fe II lines as well (Becker et al. 1997, 2000), as well as a number of quasars from the Sloan Survey (Hall et al. 2002). Finally, we ourselves have found systems of metastable Fe II absorption lines, identical to that in Arp 102B, in the BLRG 3C 332 and in the LINER NGC 1097 (Halpern 1997; Eracleous 2002).

The excitation state of the gas responsible for the Fe II absorption lines in Arp 102B is very similar to what is observed in Q 0059–2735. The absorber in the latter object has been studied in detail by Wampler et al. (1995), who suggested that it is made up of condensations in a hotter broad-absorption line flow. The temperature of the condensations is likely to be of order 10^4 K, implying that, if the metastable Fe II levels are populated by collisions, the electron density should be greater than 10^6 cm $^{-3}$. In our effort to understand the nature of the absorber in Arp 102B, we studied the X-ray spectrum obtained with the *ROSAT* PSPC and found a very large absorbing column of neutral gas, in the range $(2 - 8) \times 10^{21}$ cm $^{-2}$ (Halpern 1997). Because the *ROSAT* spectrum was so heavily absorbed, more stringent constraints could not be derived. Therefore, we observed Arp 102B with *ASCA*. This paper is devoted to the analysis and interpretation of the *ASCA* spectra, including the development and assessment of simple photoionization models for the absorbing medium. Preliminary results of this work were presented by Eracleous (2002). In §2 we describe the observations and data screening and in §3 we present the light curve and discuss the time variability. In §4 we study the X-ray continuum and determine the column density of the absorbing medium, while in §5 we derive upper limits to the equivalent width (*EW*) of the Fe K α line. In §6 we construct and evaluate simple photoionization models for the medium responsible for the UV and X-ray absorption. We discuss our findings in §7 where we examine the X-ray spectral properties of Arp 102B in the context of other BLRGs and consider the implications of the model results for the nature of the absorber. In an appendix we present the X-ray spectrum of MS 1718.6+4902, which happens to be in the field of view of Arp 102B. Throughout this paper we assume a Hubble constant of 50 km s $^{-1}$ Mpc $^{-1}$, which implies a distance to Arp 102B of 146 Mpc, given its redshift of $z = 0.0244$.

2. ASCA OBSERVATIONS AND DATA SCREENING

Arp 102B was observed with *ASCA* on 1998 February 19 with the SIS detectors in 1-CCD FAINT mode half of the time and 1-CCD BRIGHT the other half, and the GIS detectors in PH mode. It was also observed with the *ROSAT* PSPC on 1991 October 24. The exposure times and count rates are summarized in Table 1. The data were screened following standard procedures, as described in Eracleous & Halpern (1998) and in Eracleous, Halpern, & Livio (1996), with the help of the *FTOOLS/XSELECT* v. 4.2 software package (Blackburn, Greene, & Pence 1994; In-

gham 1994). After screening, we extracted spectra and light curves for each of the *ASCA* detectors as well as a *ROSAT* PSPC spectrum. In the case of the *ASCA* observations we opted to use BRIGHT mode data so that we could take advantage of the full exposure time. Although BRIGHT mode spectra represent a small compromise in spectral resolution (because the echo effect and dark-frame error are not corrected), their inclusion yields a significantly higher signal-to-noise ratio (hereafter, *S/N*).

The galaxy MS 1718.6+4902 happened to fall within the field of view of the *ROSAT* PSPC and the *ASCA* GIS during the observations of Arp 102B. For the sake of completeness, we have extracted and fitted the spectra of this source, as well. We present the results in the appendix.

3. X-RAY LIGHT CURVES AND TIME VARIABILITY

In Figure 1 we show two versions of the *ASCA* light curve, one binned in 15-minute bins and the other binned in 1-hour bins. Each light curve includes the sum of all counts from all four detectors, to maximize the *S/N*. The light curves show no obvious variability on any time scale, from the shortest time scales sampled to the length of the observation. To quantify the variability properties of Arp 102B we carried out two types of tests:

1. To search for rapid variability on time scales comparable to the light curve sampling times we compared the r.m.s. fluctuations about the mean to the average error bars in the light curve bins but found no significant fluctuations. We also computed the “excess variance,” σ_{rms} , following Nandra et al. (1997a) and Turner et al. (1999), obtaining $(1.0 \pm 0.1) \times 10^{-2}$ s $^{-1}$ for the 15-minute light curve and $(1.19 \pm 0.09) \times 10^{-2}$ s $^{-1}$ for the 1-hour light curve. For a fair comparison with Seyfert galaxies we also computed the excess variance for a light curve with 256 s bins, which gave $(2.3 \pm 0.1) \times 10^{-2}$ s $^{-1}$. The above values of the excess variance are similar to those found in Seyfert galaxies of comparable luminosity ($L_{2-10 \text{ keV}} \approx 3 \times 10^{43}$ erg s $^{-1}$; see §4) by Nandra et al. (1997a).
2. To search for long-term variations, on time scales comparable to the length of the observation, we fitted the light curves with polynomials looking for the lowest order that could provide an acceptable fit. We found that the light curves are consistent with a constant.

Finally, we searched for variability on much longer time scales by comparing our measured flux with previous measurements. By fitting the *ASCA* and *ROSAT* spectra (see next section and Table 2) we find that the 1 keV flux density increased by a factor of 3 between 1991 and 1999. Similarly, an X-ray observation with the *Einstein* IPC from 1980 (Biermann et al. 1981) shows the 1 keV flux density to be 40% lower than the 1991 *ROSAT* measurement.

4. MODEL FITS TO THE X-RAY CONTINUUM AND DETERMINATION OF ABSORPTION

The observed spectra of counts *vs* energy channel were fitted with continuum models to determine their shape and to measure the column density of absorbing material along

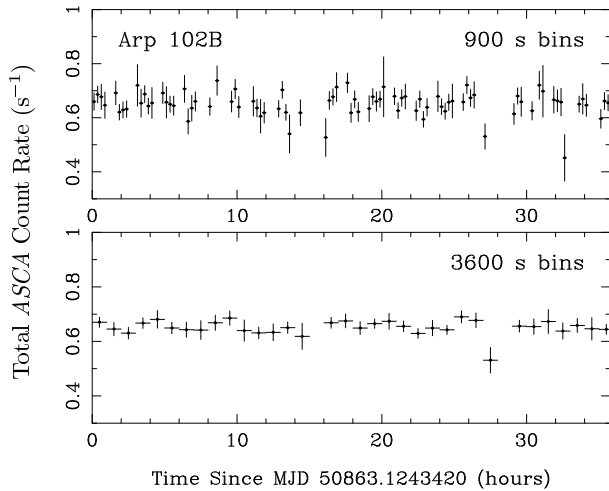


FIG. 1.— *ASCA* light curves of Arp 102B binned in (a) 15-minute bins and (b) 1-hour bins. Each light curve shows the sum of counts detected by all *ASCA* detectors.

the line of sight.³ In our first attempt to fit the *ASCA* spectra, with a simple model of a power law modified by interstellar photoelectric absorption, we found a significant discrepancy between the SIS 1 spectrum and the spectra from the other three detectors at low energies. To remedy this discrepancy, which is the result of a progressive degradation of the SIS 1 sensitivity at low energies (Yaqoob et al. 2000), we ignored all of the SIS 1 energy channels at energies below 1.2 keV. By taking this measure, we were able to reconcile the results of fits to individual spectra. We were also able to fit all spectra simultaneously with common model parameters, allowing the normalization constants of individual spectra to vary freely, to take account of uncertainties in the absolute sensitivities of the four detectors. This simple power-law model provides a good description of the observed spectrum, with a relatively flat spectral index of $\Gamma = 1.58 \pm 0.04$ and a high absorbing column density of $N_{\text{H}} = (2.8 \pm 0.3) \times 10^{21} \text{ cm}^{-2}$ (error bars correspond to the 90% confidence level; see Table 2). The spectra, with models superposed are shown in Figure 2. This column is at least an order of magnitude larger than the Galactic column. The Galactic reddening towards Arp 102B is $E(B - V) = 0.024$ (Schlegel, Finkbeiner, & Davis 1998), which implies an equivalent H I column of $N_{\text{H}}^{\text{Gal}} = 1.5 \times 10^{20} \text{ cm}^{-2}$, while measurements of the H I 21 cm line intensity towards Arp 102B yield $N_{\text{H}}^{\text{Gal}} = 2.3 \times 10^{20} \text{ cm}^{-2}$ (Stark et al. 1992). The measured 2–10 keV flux from this model is $F_{2-10 \text{ keV}} = 1.2 \times 10^{-11} \text{ erg cm}^{-2} \text{ s}^{-1}$, which af-

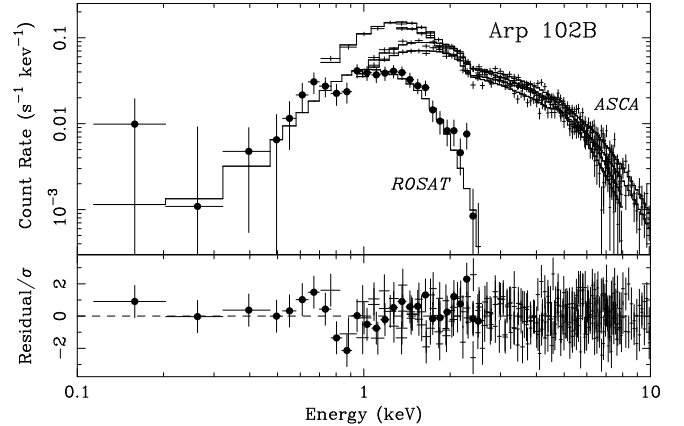


FIG. 2.— The upper panel shows spectra from each of the *ASCA* instruments and from the *ROSAT* PSPC with the best fitting model superposed. The lower panel shows the residuals after subtraction of the model from the observed spectra scaled by the error bar at each point. The model plotted here is the simple power-law model that provides the best fit to the *ASCA* spectra, with parameters as listed in Table 2. The same model has been rescaled and superposed on the *ROSAT* spectrum.

ter correcting for absorption yields an intrinsic luminosity of $L_{2-10 \text{ keV}} = 3.1 \times 10^{43} \text{ erg s}^{-1}$ (see Table 2).

Since the absorbing column density is central to our scientific goals, we explored alternative continuum models in order to determine the range of viable values. In particular, we fitted the continuum with a broken power-law model to describe a possible soft excess (inspired by Woźniak et al. 1998) and with a Compton “reflection” model to describe a possible hard excess. In Table 2 we summarize the parameters from the best fits. In fitting the broken power-law model we constrained the break energy to lie between 1 and 4 keV, based on the results of Woźniak et al. (1998). We find that the spectral indices above and below the break converge to values that are equal to each other, within uncertainties, indicating that there is no real break in the spectrum. However, the additional freedom allowed by this model over the simple power-law model results in a wider range of acceptable values of the column density. In fitting the Compton “reflection” model we employed the PEXRAV routine available within XSPEC, which computes the “reflected” spectrum as a function of the inclination of the reprocessing slab by making use of the transfer functions of Magdziarz & Zdziarski (1995). We assumed that the primary X-ray spectrum incident on the reprocessor cuts off at 100 keV and that the heavy elements in the reprocessor have Solar abundances. Thus the free parameters of the model, in addition to the photon index and absorbing column density, are the inclination angle

³ We carried out the fits with the help of the XSPEC v.10 software package (Arnaud 1996). We used version 4 (1995 March 3) of the GIS response matrices and we generated SIS response matrices appropriate for this particular observation using the SISRMG tool. To describe interstellar photoelectric absorption, we adopted the cross-sections of Morrison & McCammon (1983) and assumed that the heavy elements have Solar abundances.

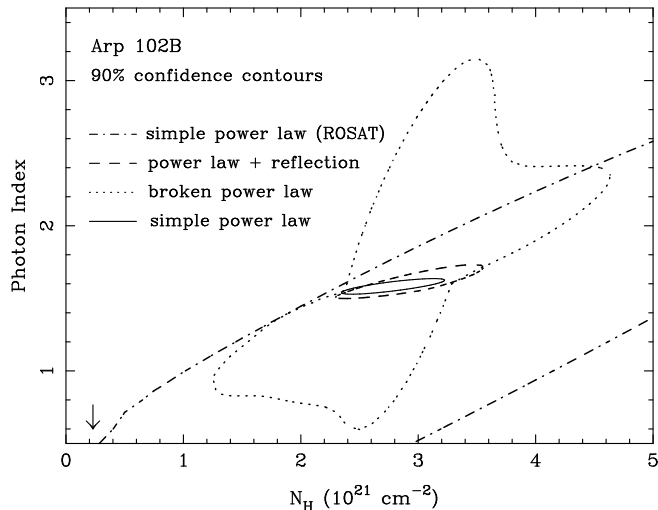


FIG. 3.— Contours showing the 90% confidence region in the $\Gamma - N_{\text{H}}$ plane. Different line styles identify contours obtained from different continuum models or different epochs, as follows: *solid line*; simple power law fit to *ASCA* spectra; *dashed line*, simple power law plus Compton “reflection” fit to *ASCA* spectra; *dotted line*, broken power law fit to *ASCA* spectra; *dot-dashed line*, simple power law fit to *ROSAT* spectrum. In the case of the broken power law model the photon index applies to the low-energy part of the spectrum, below the break. The arrow in the lower left corner marks the Galactic column density in the direction of Arp 102B.

of the reprocessing slab to the line of sight, and the solid angle it subtends to the primary X-ray source. We find that this model yields a very similar power-law index and absorbing column density to the simple power-law model. The inclination and solid angle of the reprocessing slab are virtually unconstrained. This is hardly a surprise since the most pronounced contribution of reprocessed X-rays is at energies higher than 10 keV, which falls outside of the *ASCA* bandpass. The regions of the $N_{\text{H}} - \Gamma$ parameter space allowed by each of the above models (at 90% confidence) are shown in Figure 3. We note that although the region allowed by the broken power-law model is considerably larger than those of the other two models, the minimum allowed column density of $1.3 \times 10^{21} \text{ cm}^{-2}$ is still well above the Galactic column density. In conclusion, we note that neither of the alternatives to the simple power-law model provides a better fit to the observed spectra (see the χ^2 values in Table 2). Therefore, we prefer the simple power-law model because it has the fewest free parameters. This conclusion is bolstered by the fact that the spectra of other BLRGs, observed up to 100 keV with *RXTE* do not show strong reflection components (Eracleous, Sambruna, & Mushotzky 2000). In fact, in half of the cases the 4–100 keV spectra are well-described by a simple power law.

The *ROSAT* PSPC spectrum of Arp 102B, originally presented and discussed by Halpern (1997), has a lower *S/N* than the *ASCA* spectra because of the heavy absorption and the soft bandpass of this instrument. Fitting this spectrum with an absorbed power-law model yields only an upper limit to the photon index of $\Gamma < 2.2$ and

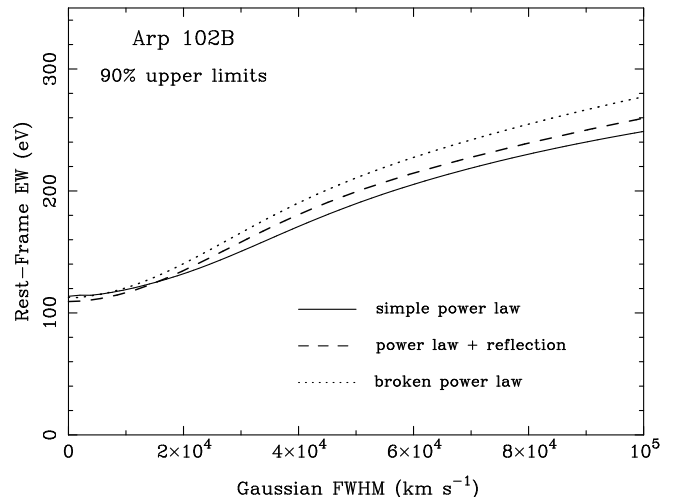


FIG. 4.— Upper limits to the equivalent width of the Fe $K\alpha$ line (at 90% confidence) as a function of the assumed velocity width of the line, for a Gaussian line profile. The three different line styles refer to different assumed models for the continuum, as follows: *solid line*, simple power law; *dashed line*, simple power law plus Compton “reflection;” *dotted line*, broken power law.

a wide range of allowed column densities, from 2×10^{20} to $5 \times 10^{21} \text{ cm}^{-2}$ (at 90% confidence). A complete list of the best-fitting model parameters is given in Table 2. The *ROSAT* PSPC spectrum is included in Figure 2, along with the *ASCA* spectra, with a rescaled version of the power-law model that fits the *ASCA* spectra superposed. The constraints derived from the *ROSAT* PSPC spectrum are plotted in Figure 3 for comparison with the constraints derived from the *ASCA* spectra. If we assume that the power-law photon index during the *ROSAT* observation was at least 1.5, then the absorbing column density must have been at least $2 \times 10^{21} \text{ cm}^{-2}$ at that time. Under the assumption that the spectral index of the *ROSAT* PSPC spectrum is the same as that of the *ASCA* spectra, we obtain an observed 0.5–2.0 keV flux of $F_{0.5-2.0 \text{ keV}} = 1.3 \times 10^{-12} \text{ erg cm}^{-2} \text{ s}^{-1}$. After correcting for absorption, this flux yields an intrinsic luminosity of $L_{0.5-2.0 \text{ keV}} = 3 \times 10^{42} \text{ erg s}^{-1}$ (see Table 2).

Finally, we also searched for absorption edges from highly ionized metals, such as O VII and O VIII, at 0.74 and 0.87 keV respectively, since measurements of, or limits on, the optical depths of these edges constrain the properties of the absorber. These edges occur at energies where the degraded SIS 1 sensitivity leads to discrepancies between the continuum model fits to the SIS 1 and SIS 0 spectra, and specifically to the inferred equivalent hydrogen column density. To bypass this problem we used the SIS 0 and SIS 1 spectra down to an energy of 0.6 keV and allowed the column densities fitted to the two spectra to be independent parameters. This way we arrive at a parametric description of the continuum, which is not physically

meaningful, but still allows us to measure discrete absorption features relative to the continuum level in both the SIS 0 and SIS 1 spectra. By adding an edge to our spectral model and scanning a range of edge rest energies between 0.7 and 0.9 keV we were able to determine the following optical depth limits at the 90% confidence level: $\tau < 0.28$ for the O VII edge and $\tau < 0.25$ for the O VIII edge.

5. THE FE $K\alpha$ LINE: TOO WEAK TO BE MEASURABLE

Since Arp 102B is notorious for its disk-like, double-peaked, optical emission lines and since the X-ray spectra of Seyfert galaxies are well-known to include disk-like Fe $K\alpha$ lines (e.g., Nandra et al. 1997b), we have looked for the Fe $K\alpha$ line in the X-ray spectrum of Arp 102B. Unfortunately, we were not able to detect it, although we were able to place interesting limits on its EW . To search for the line we fitted a model to the continuum excluding from the fit the energy range between 5 and 7 keV, where the Fe $K\alpha$ line is expected to be (assuming a rest energy of 6.4 keV). We then froze the continuum model parameters, included a Gaussian line profile in the model, and added back to the spectra the energy channels between 5 and 7 keV. To determine upper limits to the line EW we scanned the line flux–velocity dispersion parameter plane looking for regions where the model fits was acceptable, keeping the rest energy of the line fixed. Since the continuum was held fixed throughout this procedure, the resulting upper limits on the line flux can be converted to upper limits on its EW via a simple scaling. To check whether the assumed continuum model affects the results we repeated the exercise for all of the continuum models discussed in §4. Our findings are shown graphically in Figure 4, where we plot upper 90% confidence limits to the *rest* EW of the line against its assumed full width at half maximum (hereafter, FWHM). The assumed continuum model has a very small effect on the derived limits, which range from 120 eV for an unresolved line to about 200 eV for a line of FWHM comparable to that of Seyfert galaxy Fe $K\alpha$ lines (60,000 km s⁻¹; Nandra et al. 1997b). This limit is below the typical EW s measured for Seyfert galaxy Fe $K\alpha$ lines, as we discuss further in §7.1.

6. EVALUATION OF SIMPLE MODELS FOR THE UV (AND X-RAY) ABSORBER

Using the column density measured from the X-ray spectrum of Arp 102B and the properties of its UV absorption lines, we constructed simple photoionization models for the absorbing gas. The goal was to constrain the physical conditions of the absorber and its location relative to the continuum and broad-emission line sources, and deduce its role in the overall accretion flow. Previous attempts to model metastable Fe II absorbers in luminous quasars include those of Wampler et al. (1995) who studied Q 0059–2735 and of de Kool et al. (2001, 2002) who studied a number of quasars found in the FIRST survey. The above studies employed high-resolution spectra, which made possible the direct determination of the column densities of ionic species of interest and a diagnosis of the physical conditions in the absorber. Because of the low resolution of our UV spectra, we make a number of simplifying assumptions in order to construct a simple model and then

compare its predictions to the data. This exercise tests a specific hypothesis, rather than eliminating alternatives. In later sections we discuss possible observations that can lead to further tests and refinements of this model.

6.1. Limitations of the UV Spectra and Measurement of Absorption Lines

A segment of the UV spectrum of Arp 102B in the vicinity of the Mg II line, taken with the *Hubble Space Telescope* (*HST*) is shown in Figure 5, for reference. The full (1200–3200 Å) UV spectrum along with the details of the observations can be found in Halpern et al. (1996). A very serious limitation of the UV spectrum is its modest spectral resolution, which does not allow us to resolve the profiles of the absorption lines fully. As a result we cannot be certain whether the UV absorption lines are saturated, we cannot determine the kinematic structure of the absorbing gas, and we cannot unambiguously ascertain whether the absorber fully covers the continuum and broad-emission line sources (for a more extensive discussion of partial coverage see Barlow & Sargent 1997; Hamann et al. 1997; Ganguly et al. 1999). We can, nevertheless, draw indirect inferences about the above from the widths of the UV absorption lines, most importantly the lines of Mg II doublet. The observable quantities we rely on, therefore, are the EW s of the UV absorption lines, their full widths at half minimum (FWHM_{in}), and the equivalent hydrogen column density measured from the X-ray spectrum.

We measured the rest EW s and FWHM_{in} of the UV absorption lines relative to an effective continuum, defined by the combination of the true continuum and the broad emission lines on which they are superposed. The effective continuum was determined by fitting a linear combination of a low-order polynomial and one or two Gaussians to the region around the absorption lines of interest. We list the measured quantities in Table 3. A source of uncertainty is the definition of the effective continuum since the absorption lines are typically superposed on emission lines whose profiles are severely distorted by the absorption lines themselves. This is the dominant source of uncertainty in the measurements given in Table 3. We have estimated the uncertainty in EW s and FWHM_{in} by experimenting with a variety of continuum fits and noting their effect on the measured quantities. To illustrate the magnitude of these uncertainties we plot two extreme continuum fits to the peak of the Mg II line in Figure 5. These extreme fits set the extreme values of the EW s, while the best estimate is taken to be the average of the two extremes. In the case of Ly α , there is an additional source of uncertainty, which we cannot quantify: absorption by the interstellar medium in the host galaxy of Arp 120B. To deal with this issue we will treat the Ly α EW with caution in our later analysis.

The properties of the Mg II $\lambda\lambda 27896, 2803$ doublet allow us to place some constraints on the coverage fraction of the background source(s) by the absorbing gas. The FWHM_{in} we measure corresponds to a velocity of approximately 580 km s⁻¹, which is much higher than the instrumental resolution of 210 km s⁻¹. However, it is very unlikely that this broadening is due to a Gaussian internal velocity spectrum in a single parcel of absorbing gas for the following reason. We have simulated⁴ observed Mg II line

⁴ The simulation consists of synthesizing a theoretical profile for an assumed column density and kinematic broadening parameter (i.e., Gaussian

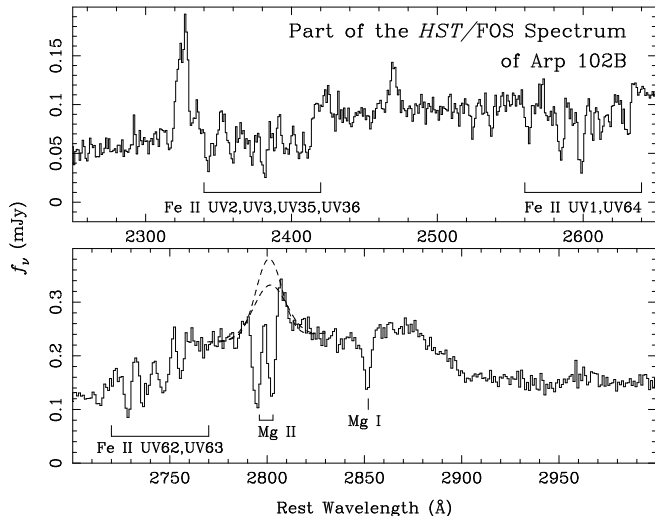


FIG. 5.— A segment of the UV spectrum of Arp 102B observed with the *HST* (Halpern et al. 1996), showing the plethora of Fe II absorption lines as well as the Mg I and Mg II absorption lines. The broad Mg II emission line and a number of narrow emission lines are also evident. The dashed lines show two extreme fits to the peak of the Mg II line, relative to which the absorption lines are measured: they illustrate the uncertainty resulting from the process of defining an effective continuum.

profiles for a range of column densities and broadening parameters (i.e., Gaussian velocity dispersions, denoted by b) and found that the lines should be fully blended if the broadening parameter was indeed as high 580 km s^{-1} , which is not observed. If, instead, we assume that the column density is so high that the lines are saturated and the kinematic broadening is small ($b < 200 \text{ km s}^{-1}$), we find that the lines are resolved and their depths are approximately equal, in very good agreement with observations. This is because the theoretical profiles of the saturated lines are approximately square so that their widths at half minimum can be large, without any blending of the wings. Further support for saturation of the Mg II doublet is provided by the observation that the two lines have nearly equal strengths even though their oscillator strengths have a ratio of 2:1. We therefore adopt the latter picture as our working hypothesis, noting the following important caveat: saturation is not necessarily the only way of reproducing the properties of the Mg II profiles. Other possibilities include a highly-ordered velocity field (as in an accelerating outflow, for example) or a clumpy absorber which gives rise to multiple “components” in the line profiles. Since neither of these possibilities can be constrained with the

velocity dispersion) and then convolving it with the instrumental line profile. The theoretical line profile is synthesized following the formalism of Humlicek (1979). The instrumental line profile is taken to be a Gaussian whose width depends on the grating-detector combination (Keys et al. 1995).

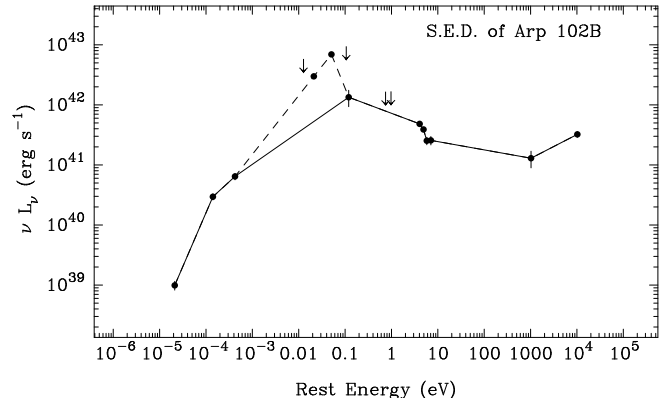


FIG. 6.— The data points show the observed spectral energy distribution (SED) of Arp 102B, which was used in our photoionization calculations. The X-ray data points at 1 and 10 keV are from the *ASCA* measurements presented here. The UV data points (between 1 and 10 eV) are from the *HST* spectrum (Halpern et al. 1996). The arrows near 1 eV are upper limits from the J- and H-band spectra of Simpson et al. (1996). All other data points are from the compilation of Chen & Halpern (1989), where references to the original papers are given. The arrows near 0.01 and 0.1 eV denote upper limits from IRAS observations at 12 and $100 \mu\text{m}$. The points connected by a solid line define the SED *without* a far-IR bump used in one of our two photoionization calculations. For the other photoionization calculation we used all of the available measurements to define an SED *with* a far-IR bump. The far-IR bump is represented by the IRAS points, which are connected by a dashed line. A more extensive discussion of the choice of SEDs is given in §6.2 of the text.

available data, we cannot explore them further.

An important consequence of the saturated Mg II lines is that the absorber must cover the background sources (continuum source and/or broad-emission line region) only partly; if it did not, the troughs of the absorption lines should have been nearly black, (i.e., they should have reached close to zero intensity, since their widths are just below the resolution limit of the instrument). From the observed depth of the lines and by comparison with our simulated profiles, we deduce a coverage fraction of $f_C \approx 0.5$, which we use to correct the measured EW of the Mg II lines (see Table 3). Carrying out the same exercise for other absorption lines ($\text{Ly}\alpha$, Si III, and Mg I) we derive comparable coverage fractions, which we also list in Table 3. Finally, we also assume a coverage fraction of 0.6 for the weaker lines for the sake of consistency. As we show later, this assumption does not affect our results or conclusions. These coverage fractions should be regarded with caution because they are inferred indirectly and only after making the assumptions that we do. An alternative possibility, for example, is that the lines originate in an outflow whose ordered velocity field leads to square absorption-line profiles. Therefore, in the analysis that follows, we

will explore both the case of finite and negligible partial coverage.

6.2. Model Assumptions and Methodology

Our main observational constraints comprise the total column density of hydrogen, determined from the X-ray spectrum, and the *EWs* of the UV absorption lines. An additional constraint is provided by the relative strengths of the Fe II absorption lines from the ground state and metastable states. More specifically, the lines of the UV1 and UV64 multiplets, which fall in a “clean” part of the UV continuum, around a rest wavelength of 2600 Å, can be used. Thus, in order to construct a model for the absorber we make the following assumptions:

- The X-ray and UV absorption arise in the same medium, therefore we seek a model that can satisfy all the observational constraints simultaneously, as far as possible.
- The absorber consists of a uniform slab of gas, which is photoionized by the continuum from the AGN central engine. This slab most likely has a bulk outflow velocity of about 200 km s⁻¹, as noted by Halpern et al. (1996), but its internal velocity dispersion is assumed to be small (< 200 km s⁻¹; see §6.1). The equivalent hydrogen column density of this slab is $N_{\text{H}} = 2.8 \times 10^{21}$ cm⁻², as measured from the *ASCA* spectra and its metallicity and abundance pattern follow those of the Sun.
- The spectral energy distribution (SED) of the ionizing continuum is the same as the observed SED, which we plot in Figure 6. We assume that the shape of the SED between 1 and 10 keV continues up to 100 keV where it cuts off exponentially. An important feature of this SED is that it has no “UV bump.” As such it closely resembles the SEDs of low-luminosity AGNs (see Ho 1999). The far-IR measurements of this SED come from IRAS observations, which were taken through a very large aperture and may not represent the true far-IR flux of the nucleus. Therefore, we repeated our calculations for two different assumed SEDs, with and without a “far-IR bump” (see illustration in Figure 6).

Under the above assumptions we computed the ionization structure of the absorbing slab using the photoionization code *Cloudy* (versions 94.00 and 95.04β3; Ferland 1996) for a wide range of values of the ionization parameter and hydrogen number density (U and n , respectively). In particular, our calculations span the range $\log U = -5.0$ to $+2.0$ in steps of 0.5 and $\log n = 2$ to 15 in steps of 1 (n is measured in cm⁻³). The code includes a detailed model of the Fe II ion (Verner et al. 1999) which yields the optical depths at line center of the Fe II transitions of interest. For each cell in the $\log U - \log n$ parameter space we obtain the column density of the ions of interest, from which we compute the *EWs* of absorption lines for an assumed broadening parameter. These are the quantities that we can compare directly with observations. By comparing the observed and predicted *EWs* of each

observed absorption line we obtain a set of constraints on $\log U$ and $\log n$, as we describe further in the next section. The lines used in this comparison are those listed in Table 3. In the second stage of our comparison of models with data, we derive additional constraints by using the relative strengths of the lines in the Fe II UV1 and UV64 multiplets and the shape of the soft X-ray spectrum.

6.3. Results and Checks for Self-Consistency

Our results are shown graphically in Figure 7, which depicts part of the $\log U - \log n$ parameter space covered by our photoionization calculations. The two different assumed SEDs give virtually identical results, therefore we describe and discuss the results below without regard to the SED. The dotted line in this figure shows the region in which the *EWs* of the Mg I, Mg II, and Fe II lines predicted by the models agree with the measured *EW*. The lower limit to the density is set by the *EW* of the Mg I λ2853 line. Thus the properties of the absorber are constrained by these lines as follows: $-3.5 < \log U < -2.5$ and $\log n \geq 11$. The models that reproduce the *EWs* of the Mg-Fe family of lines cannot reproduce the *EWs* of all the other lines of Table 3 (the Si-Al-C-H family) for a single broadening parameter. The latter family of lines requires similar densities to the former, but a somewhat higher ionization parameter, namely $-3.0 < \log U < -1.5$ and $\log n \geq 11$, as shown by the dashed line in Figure 7. If we do not consider the *EW* of Lyα (see discussion in §6.1) as one of our constraints, the Si, Al, and C do not set any limits on the density of the absorber. Inclusion of Lyα, however, does set a lower limit on the density of $\log n \geq 11$ (solid vertical bar in Figure 7) as follows: for lower densities, one can find models that reproduce the *EWs* of the Si, Al, and C lines simultaneously but fail to reproduce the *EW* of Lyα. This set of model parameters predicts a *EW* for the Mg and Fe lines that is too low compared to observations.

It is noteworthy that the above results are insensitive to the assumption of partial coverage. According to the models, all of the observed absorption lines are on the flat part of the curve of growth, therefore their theoretical *EWs* depend mostly on the broadening parameter and are relatively insensitive to the ionic column density. If we take the measured *EWs* at face value, without applying a correction for partial coverage, we find that the lines in the Mg-Fe family require $b = 80 - 100$ km s⁻¹ and the lines in the Si-Al-C-H family require $b = 90 - 130$ km s⁻¹. If, on the other hand, we adopt the coverage fractions listed in Table 3, we find that the lines in the Mg-Fe family require $b = 140 - 190$ km s⁻¹ and the lines in the Si-Al-C-H family require $b = 100 - 160$ km s⁻¹.

As a consistency test we compared the relative strengths of the lines in the Fe II UV1 and UV64 multiplets with the model predictions. These are the only useful Fe II multiplets for this test because they fall in “clean” part of the continuum, which is free of emission lines. Since the lines are severely blended, we used the optical depths predicted by the models, assumed a value for the broadening parameter and synthesized the expected spectrum, which we compared to the data. The adjustable parameters in this comparison were the broadening parameter and the coverage fraction of the background source by the absorber.

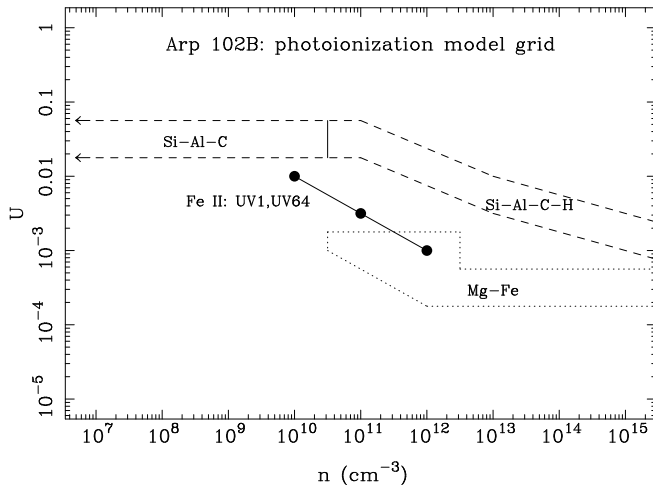


FIG. 7.— Constraints on the ionization parameter and hydrogen density from the observed absorption line *EW*s. This diagram shows a segment of the $\log U - \log n$ parameter space spanned by our photoionization calculations described in §6.2 of the text. The dotted line shows the region allowed by the *EW*s of the Mg, and Fe lines. The dashed line shows the region allowed by the *EW*s of the Si, Al, and C lines (no density constraints; labeled as Si-Al-C). If the *EW* of Ly α is used as an additional constraint, only the part of this region on the right of the solid vertical bar is allowed ($\log n \geq 11$; labeled as Si-Al-C-H). The filled circles connected by a solid line mark the grid cells for which the predicted spectrum of the Fe II UV1 and UV64 multiplets is in reasonable agreement with the data (see Figure 8). The SEDs with and without a far-IR bump produce virtually identical results.

We searched the parameter region defined by $\log U = -2.0$ to -3.5 and $\log n = 10$ to 15 and found reasonable, although not perfect, agreement for the following parameter sets: $(\log U, \log n) = (-2.0, 10)$, $(-2.5, 11)$, $(-3.0, 12)$ and coverage fractions between 0.7 and 0.8. These parameter sets are indicated in Figure 7 with large filled circles connected by a solid line. The best agreement between the observed and predicted spectrum is achieved for $(\log U, \log n) = (-3.0, 12)$, $b = 180 \text{ km s}^{-1}$, and $f_C = 0.7$. The predicted spectrum resulting from this model is compared to the observed spectrum in Figure 8, where the lines from the Fe II UV1 and UV64 multiplets are marked. We note that in Figure 8, the relative strengths of the strongest lines from each multiplet ($\lambda 2600$ from UV1 and $\lambda 2563$ from UV64) agree fairly well with the data, but the relative strengths of lines within a multiplet do not.⁵ At $\log n < 10$ or $\log U < -3.5$, the optical depths of these lines are so large that they blend together. At $\log n > 12$ the lines become rather weak due to collisional ionization of Fe II to Fe III and their predicted relative strengths are in very poor agreement with the observations.

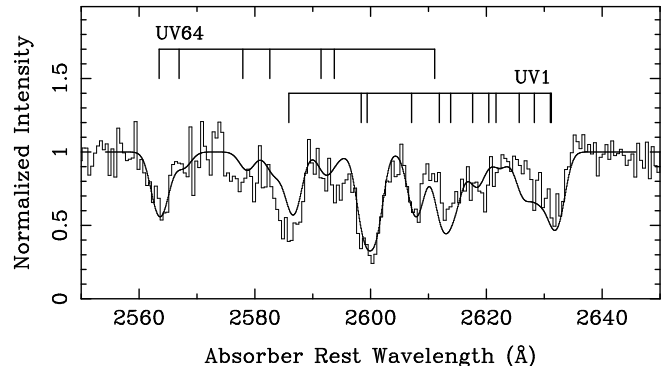


FIG. 8.— Comparison of the predicted spectrum of the Fe II UV1 and UV64 multiplets (smooth line), with the normalized spectrum of Arp 102B. The theoretical spectrum corresponds to a model with $\log U = -3$ and $\log n = 12$, with broadening parameter $b = 180 \text{ km s}^{-1}$ and a coverage fraction $f_C = 0.7$. The locations of the lines from each multiplet are identified. The wavelength scale refers to the rest frame of the absorber, which is blueshifted by 150 km s^{-1} relative to the frame of the narrow emission lines of Arp 102B.

Additional consistency tests are afforded by the X-ray spectrum and in particular, by the observed equivalent neutral hydrogen column density and the absence of absorption edges from highly-ionized metals. The models that best explain the UV absorption lines predict that the elements that contribute to the soft X-ray absorption (0.1–1 keV; see Morrison & McCammon 1983), namely C, N, and O, retain their K-shell electrons and can act as effective absorbers. For example, at $\log U = -3.0$ the dominant ionization stages of these elements are C I, C II, N I, N II, O II, and O III. At $\log U = -1.5$, however, an appreciable fraction of C and N atoms become fully ionized, which reduces the soft X-ray opacity and an appreciable fraction of the O atoms are in the form of O VII and O VIII. This results in strong absorption edges at 0.74 and 0.87 keV respectively. Therefore, the X-ray spectrum constrains the ionization parameter to values of $\log U \leq -2.0$, where soft X-ray absorption by metals is appreciable and the optical depths of O VII and O VIII K-shell edges are below our observed upper limits (see §4). At the lowest X-ray energies of the *ROSAT* spectrum (0.1–0.2 keV), the

⁵ This could be a consequence of one or more of the following factors: (a) Blending of some of the Fe II lines of Arp 102B with Galactic Fe II lines. As shown in Halpern et al. (1996), some weak Fe II UV1 lines at $z = 0$ overlap with some of the Fe II UV64 lines at $z = 0.0244$. This is a minor effect, however, and cannot explain the discrepancy fully. (b) Coarse temperature or density sampling in our model grid. These multiplets could conceivably provide much finer constraints on the temperature and density, but the necessary computations are prohibitively expensive. (c) The Fe II oscillator strengths used by Cloudy, which are taken from the Iron Project (Nahar 1995) may not be quite correct. de Kool et al. (2001) compared measured and calculated Fe II oscillator strengths from various sources and found significant outliers among the Iron Project values. An inspection of their Table 2 shows a marked correspondence between the poorly-fitting lines in our Figure 8 and the discrepant oscillator strengths.

opacity is dominated by photoelectric absorption by He, which at the densities of interest, is mostly in the form of He II and He III at $\log U \geq -2.5$ and mostly in the form of He I and He II at $\log U \leq -3.0$. This implies that the soft X-ray flux should start to recover from absorption at such low energies. Unfortunately, the poor S/N of the *ROSAT* spectrum at these low energies does not allow us to check this prediction, although the shape of the spectrum is suggestive of an upturn at 0.1–0.2 keV (see Figure 2).

7. DISCUSSION AND CONCLUSIONS

7.1. *The X-Ray Spectral Properties of Arp 102B in Context*

The X-ray properties of Arp 102B reinforce previously known trends of systematic differences between Seyfert galaxies and BLRGs. As we have already remarked, simple power-law spectra, with neither a soft nor a hard excess are fairly common among BLRGs observed with *ASCA*, *RXTE*, *BeppoSAX*, and *Ginga* (Woźniak et al. 1998; Sambruna et al. 1999; Hasenkopf, Sambruna, & Eracleous 2002; Eracleous et al. 2000; Grandi, Urry, & Maraschi 2002; Zdziarski et al. 1995). Seyferts, on the other hand, often show a soft and/or a hard excess in their spectra. The heavy absorption by “cold” (i.e. neutral) matter found in Arp 102B is not uncommon in radio-loud AGNs, in contrast to Seyfert 1 galaxies whose spectra often show the signature of a “warm” (i.e., ionized) absorber (Reynolds 1997; George et al. 1998; Kaspi et al. 2000). Sambruna et al. (1999) find such heavy absorption in 1/3 of the BLRGs and radio-loud quasars in their collection, with columns of 10^{21} cm^{-2} , or higher (see their Figure 6).

The relatively flat spectral index of Arp 102B, although not typical of luminous BLRGs (e.g., 3C 390.3, 3C 111, 3C 120, 3C 382) is characteristic of a subclass of radio-loud AGNs, the weak-line radio galaxies (hereafter WLRGs; see Sambruna et al. 1999 for a summary of their X-ray properties). These are radio galaxies distinguished by the low luminosity of their [O III] $\lambda 5007$ emission lines (Tadhunter et al. 1998; Laing et al. 1994). The combination of spectral index and X-ray luminosity of Arp 102B puts it well within the region occupied by WLRGs in Figure 2d of Sambruna et al. (1999). Moreover, its [O III] $\lambda 5007$ emission-line luminosity of $9.6 \times 10^{40} \text{ erg s}^{-1}$ is comparable to the [O III] luminosities of WLRGs, although its integrated 0.1–100 GHz radio luminosity is an order of magnitude lower than the least luminous WLRGs in the Tadhunter et al. (1998) sample.

The weakness of the broad, disk-like Fe $K\alpha$ line compared to Seyferts appears to be a hallmark of BLRGs as a class (Woźniak et al. 1998; Sambruna et al. 1999; Eracleous et al. 2000). This difference is illustrated in Figure 6 of Hasenkopf et al. (2002), where the locations of Seyfert galaxies and BLRGs in the Fe $K\alpha$ $EW - L_{2-10 \text{ keV}}$ plane are compared. In the vast majority of cases, BLRGs fall below the region occupied by Seyferts, with Arp 102B representing the lowest-luminosity BLRG with available data. The weakness of the Fe $K\alpha$ line of Arp 102B can be understood if the inner accretion disk has the form of an ion torus or ADAF, rather than a thin disk surrounded by a hot corona, as is thought to be the case in Seyfert galaxies (Haardt & Maraschi 1993; Haardt, Maraschi, & Ghisellini

1994). The geometry of an optically thin, vertically extended inner disk illuminating a geometrically thin, dense outer disk reduces the available solid angle of the fluorescing medium (the thin disk) by a factor of 2 relative to a thin disk sandwiched by a hot corona (Chen & Halpern 1989; Zdziarski, Lubiński, & Smith 1999) and results in a reduction of the the Fe $K\alpha$ EW by the same factor. This picture is also appealing because it explains some of the other properties of Arp 102B (e.g., the optical double-peaked emission lines and the shape of the SED; see Chen & Halpern 1989) and because it may be applicable to other low-luminosity BLRGs (Eracleous et al. 2000). For example, 3C 332 is a dead-ringer for Arp 102B: not only does it have a highly-absorbed X-ray spectrum and an X-ray luminosity similar to that of Arp 102B (Crawford & Fabian 1995), but it also sports optical double-peaked emission lines and metastable Fe II absorption lines in the UV.

The above discussion refers to the extremely broad, disk-like Fe $K\alpha$ lines found in the *ASCA* spectra of Seyfert galaxies. However, recent observations of bright Seyfert galaxies at high spectral resolution (with the *Chandra* grating spectrometers) or at high S/N (with the *XMM-Newton* CCD cameras) have shown that the lines can be decomposed into a broad, disk-like component and a narrower, bell-shaped component. Examples include NGC 3783 (Kaspi et al. 2002), NGC 5548 (Yaqoob et al. 2002a), and NGC 3516 (Turner et al. 2002; Netzer et al. 2002). The narrower component has a width of a few thousand km s^{-1} and can be plausibly attributed to the “broad-line region,” which is the source of the broad, optical emission lines. The EW of the narrower component is typically around 90–130 eV. Such lines would not be detectable in the *ASCA* spectrum of Arp 102B, since their EW s are just below the detection limit.

7.2. *Constraints on the Absorber, Implications, and Future Prospects*

In summary, we find that simple, single-zone models for the absorber require high densities of $n \geq 10^{11} \text{ cm}^{-3}$. However, not all UV absorption lines can be produced at the same ionization parameter: the Fe and Mg lines require an ionization parameter in the range $10^{-3.5} < U < 10^{-2.5}$, while the Si, Al, C, and H lines require a higher ionization parameter of $10^{-3.0} < U < 10^{-1.5}$ (the two regions of parameter space do not overlap, however, as illustrated in Figure 7). The models that reproduce the EW s of the Si, Al, C, and H lines predict Mg and Fe line EW s that are much lower than the observed values, and *vice-versa*: the models that reproduce the EW s of the Mg and Fe lines predict Si, Al, C, and H line EW s that are much lower than the observed values. The models that explain the Mg-Fe absorber can also explain the X-ray absorption observed in the *ASCA* and *ROSAT* spectra. Including a “far-IR bump” in the SED has a negligible effect on these conclusions.

The simple, single-zone models that we have considered, although partially successful, do not provide a fully satisfactory description of the absorber. One possible way out of this difficulty would be to adjust the abundances of Mg and Fe relative to the other elements by a factor of a few. However, more sophisticated models are probably necessary and higher-resolution spectra are sorely needed

to constrain them and guide their development. One possible effect that an improved model could incorporate is radiative transfer in an accelerating medium, since it may play a role in determining the strengths of the absorption lines. This could be an important effect, if the absorber has the form of an outflowing wind. Another possibility relevant to the outflowing wind scenario is that the absorber spans a range of densities or that it contains pockets or layers of higher or lower density gas. Such a structure could lead to the two phases that are apparently needed to explain the strengths of the observed absorption lines. Different phases or layers of the absorber may reveal themselves in the form of “components” of the line profiles in high-resolution UV spectra. In this sense, our preferred model for the Mg-Fe absorber is reminiscent of the model of Kraemer et al. (2001) for NGC 4151: their high-resolution spectra allowed them decompose the absorber into distinct kinematic components, one of which was responsible for the metastable Fe II absorption lines. Their photoionization model for this particular component required a high density of $n \geq 10^{9.5} \text{ cm}^{-3}$, an ionization parameter of $U = 10^{-1.8}$, and a high column density of $N_{\text{H}} \approx 3 \times 10^{21} \text{ cm}^{-2}$. Their interpretation was that this component of the absorber was the closest to the ionizing source.

Examining the model results from a broader perspective and comparing them with results of detailed models of absorption lines in Seyfert galaxies, we find that a range of ionization parameters in the absorbing gas is not at all uncommon; in fact, it is the rule rather than the exception. This conclusion follows from studies of the UV and X-ray absorption lines in bright Seyfert galaxies such as NGC 3783 (Kaspi et al. 2001; Blustin et al. 2002), NGC 5548 (Crenshaw & Kraemer 1999; Kaastra et al. 2002), NGC 4051 (Collinge et al. 2001), IRAS 13349+2438 (Sako et al. 2001), NGC 3516 (Kraemer et al. 2002a), and Mrk 509 (Yaqoob et al. 2002b; Kraemer et al. 2002b) using high-resolution spectra. More specifically, the UV absorption lines, and sometimes even the X-ray lines, can be decomposed into several kinematic components, which require gas with a wide range of ionization parameters (this is sometimes obvious from a simple comparison of the line profiles, without the need for detailed modeling). In other cases a wide range of ionization is inferred with the help of photoionization models: such models cannot reproduce the strengths of all of the observed lines under the assumption of a uniform absorber with a single ionization parameter. What is different between Arp 102B and Seyfert galaxies, however, is the presence of metastable Fe II absorption lines and the requirement for high densities to explain them. As we have noted in previous sections, such lines are rare in Seyfert galaxies.

Taking the properties of the absorber in Arp 102B inferred from the models at face value, we may deduce its distance from the source of ionizing radiation. We find that the absorber distance is related to the model parameters via $r = 7 \times 10^{16} (U_{-3} n_{11})^{-1/2} \text{ cm}$ (where $U_{-3} = U/10^{-3}$ and $n_{11} = n/10^{11} \text{ cm}^{-3}$). Since $U = 10^{-3.0}$ and $n = 10^{11} \text{ cm}^{-3}$ represent the lowest allowed photon flux incident on the face of the absorber, the absorber distance should be less than $7 \times 10^{16} \text{ cm}$. We can recast this limit in terms of the gravitational radius,

$r_{\text{g}} \equiv GM_{\bullet}/c^2$ (where M_{\bullet} is the mass of the central black hole), as $r/r_{\text{g}} \lesssim 5,000 (U_{-3} n_{11})^{-1/2} M_8^{-1}$ (where $M_8 = M_{\bullet}/10^8 M_{\odot}$). This distance is slightly larger than the size line-emitting portion of the disk, inferred from fits to the profiles of the broad Balmer emission lines, which extends over the range $r/r_{\text{g}} = 500 - 1,000$ (Chen et al. 1989; Chen & Halpern 1989). We may also estimate the thickness of the absorber along the line of sight as $\delta r \sim N_{\text{H}}/n$, which gives $\delta r \lesssim 3 \times 10^{10} \text{ cm}$, or $\delta r/r_{\text{g}} \lesssim 2 \times 10^{-3} M_8^{-1}$, assuming that $n \geq 10^{11} \text{ cm}^{-3}$. Comparing the Fe II absorber in Arp 102B with those in luminous quasars, we find it to be quite different: it is more dense and located closer to the ionizing source. In comparison, the Fe II absorber in Q 0059-2735 has $10^6 \text{ cm}^{-3} < n < 10^8 \text{ cm}^{-3}$ and $2.4 \times 10^5 M_8^{-1} \lesssim r/r_{\text{g}} \lesssim 1.3 \times 10^6 M_8^{-1}$ (Wampler et al. 1995), while in the FIRST quasars studied by de Kool et al. (2001, 2002) the Fe II absorber is characterized by $n \sim 10^3 - 10^5 \text{ cm}^{-3}$ and $r/r_{\text{g}} \sim 10^8 M_8^{-1}$.

Independently of the model results, there are two more hints afforded by the data: (1) the absorbing material is either outside of the broad-line region or mixed in with it, since the Mg II absorption lines are deeper than the broad Mg II *emission* lines, and (2) the dust-to-gas ratio in the absorber is rather low, since for a Galactic dust-to-gas ratio we would expect a reddening of $E(B - V) = 0.43$, which would strongly attenuate the broad UV emission lines, contrary to what is observed (Halpern et al. 1996). Putting all the clues together, it is plausible to think of the absorber as thin, dense sheets or filaments embedded in an outflowing wind overlaying the outer accretion disk, which is thought to be the source of the broad, double-peaked emission lines of Arp 102B. This outflowing wind may also be the source of the broad UV high-ionization and Ly α emission lines (see the general discussion by Collin-Souffrin & Dumont 1989, and references therein, and the specific discussion of Arp 102B by Halpern et al. 1996). A very similar scenario may apply to other AGNs of relatively low luminosity, which have many properties in common with Arp 102B, including Fe II absorption lines in their UV spectra, for example the BLRG 3C 332 and the LINER NGC 1097 (Halpern 1997; Eracleous 2002).

We are grateful to Gary Ferland for his patience and invaluable help with the photoionization code Cloudy. We also thank Chris Churchill for his help in developing some of the software tools for this work and the anonymous referee for thoughtful comments and suggestions. This work was supported by NASA through grants NAG5-10817 and NAG5-8369.

REFERENCES

- Arnaud, K. 1996, in ASP Conf. Ser. 101, *Astronomical Data Analysis Software and Systems V*, eds. G. Jacoby & J. Barnes (San Francisco: ASP), 17
- Barlow, T. A. & Sargent, W. L. W. 1997, *AJ*, 113, 136
- Becker, R. H., Gregg, M. D., Hook, I. M., McMahon, R. G., White, R. L., & Helfand, D. J. 1997, *ApJ*, 479, L93
- Becker, R. H., White, R. L., Gregg, M. D., Brotherton, M. S., Laurent-Muehleisen, S. A., & Arav, N. 2000, *ApJ*, 538, 72
- Becker, R. H., White, R. L., Helfand, D. J. 1995, *ApJ*, 450, 559
- Biermann, P., Preuss, E., Kronberg, P. P., Schilizzi, R. T., & Shaffer, D. B. 1981, *ApJ*, 250, L49
- Blackburn, J. K., Greene, E. A., & Pence, B. 1994, *User's Guide to FT00LS* (Greenbelt: GSFC)
- Blustin A. J., Branduardi-Raymont, G., Behar, E., Kaastra, J., Kahn, S. M., Page, M. J., Sako, M., & Steenbrugge, K. C. 2002, *A&A* 392, 453
- Boroson, T. A., Meyers, K. A., & Morris, S. L. 1991, *ApJ*, 370, L19
- Chen, K., Halpern, J. P., & Filippenko, A. V. 1989, *ApJ*, 339, 742
- Chen, K. & Halpern J. P. 1989, *ApJ*, 344, 115
- Collinge, M. J. et al. 2001, *ApJ*, 557, 2
- Collin-Souffrin, S. & Dumont, A. M. 1989, *A&A* 213, 29
- Cowie, L. L., et al. 1994, *ApJ*, 432, L83
- Crawford, C. S. & Fabian, A. C. 1995, *MNRAS*, 273, 827
- Crenshaw, D. M. & Kraemer, S. B. 1999, *ApJ*, 521, 572
- Crenshaw, D. M., Kraemer, S. B., Bruchweiler, F. D., & Ruiz, J. R. 2001, *ApJ*, 555, 633
- Eracleous, M. 1998, *Adv. Sp. Res.*, 21, 33
- Eracleous, M. 1999, in *Structure and Kinematics of Quasar Broad-Line Regions*, ASP Conf. Ser. 175, eds C. M. Gaskell et al. (San Francisco: ASP), 163
- Eracleous, M. 2002, in *Mass Outflow in Active Galactic Nuclei: New Perspectives*, ASP Conf. Ser. 255, , eds. D. M. Crenshaw, S. B. Kraemer, & I. M. George (San Francisco: ASP), 132
- Eracleous, M. & Halpern, J. P. 1994, *ApJS*, 90, 1
- Eracleous, M. & Halpern, J. P. 1998, *ApJ*, 505, 577
- Eracleous, M., Halpern, J. P., & Livio, M. 1996, *ApJ*, 459, 89
- Eracleous, M., Sambruna, R. M., & Mushotzky, R. F. 2000, *ApJ*, 537, 654
- Ferland, G. J. 1996, *Hazy, a Brief Introduction to Cloudy*, University of Kentucky, Department of Physics and Astronomy Internal Report
- George, I. M., Turner, T. J., Netzer, H., Nandra, K., Mushotzky, R. F., & Yaqoob, T. 1998, *ApJS*, 114, 73
- Ganguly, R., Eracleous, M., Charlton, J. C., & Churchill, C. W. 1999, *A.J.*, 117, 2594
- Grandi, P., Urry, C. M., & Maraschi, L. 2002, *New Astr. Rev.* 46, 221
- Haardt, F. & Maraschi, L. 1993, *ApJ*, 413, 507
- Haardt, F., Maraschi, L., & Ghisellini, G. 1994, *ApJ*, 432, L95
- Hall, P. B., et al. 2002, in *Mass Outflow in Active Galactic Nuclei: New Perspectives*, ASP Conf. Ser. 255, , eds. D. M. Crenshaw, S. B. Kraemer, & I. M. George (San Francisco: ASP), 161
- Halpern, J. P. 1997, in *Mass Ejection from Active Galactic Nuclei*, ASP Conf. Ser. 128, eds, N. Arav, I. Shlosman, & R. J. Weymann, (San Francisco: ASP), 41
- Halpern J. P., Eracleous, M., Filippenko, J. P., & Chen, K. 1996, *ApJ*, 464, 704
- Hamann, F., Barlow, T. A., Junkkarinen, V. & Burbidge, E. M. 1997a, *ApJ*, 478, 80
- Hasenkopf, C. A. Sambruna, R. M., & Eracleous, M. 2002, *ApJ*, 575, in press (astro-ph/0204257)
- Hazard, C., McMahon, R. G., Webb, J. K., Morton, D. C. 1987, *ApJ*, 323, 263
- Ho, L. C. 1999, *ApJ*, 516, 672
- Humlicek, J. 1979, *J. Quant. Spectrosc. Radiat. Transfer*, 21, 309
- Ingham, J. 1994, *The XSELECT User's Guide* (Greenbelt: GSFC)
- Kaastra, J. S., Steenbrugge, K. C., Raassen, A. J. J., van der Meer, R. L. J., Brinkman, A. C., Liedahl, D. A., Behar, E., & de Rosa, A. 2002, *A&A*, 386, 427
- Kaspi, S., Brandt, W. N., Netzer, H., Sambruna, R., Chartas, G., Garmire, G., & Nousek, J. A. 2000, *ApJ*, 535 L17
- Kaspi, S. et al 2001, *ApJ*, 554, 216
- Kaspi, S. et al 2002, *ApJ*, 574, 643
- de Kool, M., et al. 2001, *ApJ*, 548, 609
- de Kool, M., et al. 2002, in *Mass Outflow in Active Galactic Nuclei: New Perspectives*, ASP Conf. Ser. 255, , eds. D. M. Crenshaw, S. B. Kraemer, & I. M. George (San Francisco: ASP), 183
- Keys, C. D., Koratkar, A. P., Dahlem, M., Hayes, J., Christensen, J., & Martin, S. 1995, *Faint Object Spectrograph Instrument Handbook Version 6.0* (Baltimore: Space Telescope Science Institute)
- Kraemer, S. B., et al 2001, *ApJ*, 551, 671
- Kraemer, S. B., Crenshaw, M., George, I. M., Netzer, H., Turner, T. J., & Gable, J., 2002, *ApJ*, in press (astro-ph/0205389)
- Kraemer, S. B., Crenshaw, M., Yaqoob, T., McKernan, B., Gable, J., George, I. M., Turner, T. J., & Dunn, J. P. 2002, *ApJ*, in press (astro-ph/0208478)
- Kriss, G. A., Davidsen, A. F., Zheng, W., Kruk, J. W., & Espey, B. R. 1995, *ApJ*, 454, L7
- Laing, R. A., Jenkins, C. R., Wall, J. V., & Unger, S. W. 1994 in *ASP Conf. Ser. 54, The First Stromlo Symposium: The Physics of Active Galaxies*, ed. G. Bicknell, M. A. Dopita, & P. J. Quinn, (San Francisco: ASP), 201
- Maccacaro, T., della Ceca, R., Gioia, I. M., Morris, S. L., Stocke, J. T., & Wolter, A. 1991, *ApJ*, 374, 117
- Magdziarz, P., & Zdziarski, A. A. 1995, *MNRAS*, 273, 837
- Morrison, R. & McCammon, D. 1983, *ApJ*, 270, 119
- Nahar, S. 1995, *A&A*, 293, 967
- Nandra, K., George, I. M., Mushotzky, R. F., Turner, T. J., & Yaqoob, T. 1997a, *ApJ*, 476, 70
- Nandra, K., George, I. M., Mushotzky, R. F., Turner, T. J., & Yaqoob, T. 1997b, *ApJ*, 477, 602
- Narayan, R. & Yi, I. 1994, *ApJ*, 428, L13
- Narayan, R. & Yi, I. 1995, *ApJ*, 444, 231
- Netzer, H., Chelouche, D., George, I. M., Turner, T. J., Crenshaw, D. M., Kraemer, S. B., & Nandra, K. 2002, 571, 256
- Rees, M. J., Begelman, M. C., Blandford, R. D., & Phinney, E. S. 1982, *Nature*, 295, 17
- Reynolds C. S., 1997, *MNRAS*, 286, 513
- Sambruna, R. M., Eracleous, M., & Mushotzky, R. F. 1999, *ApJ*, 526, 60
- Sako, M. et al. 2001, *A&A*, 365, 168
- Schlegel, D. J., Finkbeiner, D. P., & Davis, M. 1998, *ApJ*, 500, 525
- Simpson, C., Forbes, D. A., Baker, A. C., & Ward, M. J. 1996, *MNRAS*, 283, 777
- Smith, P. S., Schmidt, G. D., Allen, R. G., Angel, J. R. P. 1995, *ApJ*, 444, 146
- Stark, A. A., Gammie, C. F., Wilson, R. W., Bally, J., Linke, R. A., Heiles, C., & Hurwitz, M. 1992, *ApJS*, 79, 77
- Stauffer, J., Schild, R., & Keel, W. C. 1983, *ApJ*, 270, 465
- Stocke, J. T., Morris, S. L., Gioia, I. M., Maccacaro, T., Schild, R., Wolter, A., Fleming, Thomas A., & Henry, J. P. 1991, *ApJS*, 76, 813
- Tadhunter, C. N., Morganti, R., Robinson, A., Dickson, R., Villarmartin, M., Fosbury, R. A. E. 1998, *MNRAS*, 298, 1035
- Turner, T. J., George, I. M., Nandra, K., Turcan, D. 1999, *ApJ*, 524, 667
- Turner, T. J. et al. 2002, *ApJ*, 574, L123
- Verner, E. M., Verner, D. A., Korista, K. T., Ferguson, J. W., Hamann, F., & Ferland, G. J. 1999, *ApJS*, 120, 101
- Wampler, E. J., Chugai, N. N., & Petitjean, P. 1995, *ApJ*, 443, 586
- Woźniak, P. R., Zdziarski, A. A., Smith, D., Madejski, G. M., & Johnson, W. N. 1998, *MNRAS*, 299, 449
- Yaqoob, T., et al. 2000, *ASCA GOF Calibration Memo ASCA-CAL-00-06-01, v1.0*, <http://heasarc.gsfc.nasa.gov/docs/asca/calibration/nhparam.html>
- Yaqoob, T., George, I. M., Nandra, K., Turner, T. J., Serlemitsos, P. J., & Mushotzky, R. F. 2002a, *ApJ*, 571, 256
- Yaqoob, T., McKernan, B., Kraemer, S. B., Crenshaw, M., Gable, J., George, I. M., & Turner, T. J. 2002b, *ApJ*, in press (astro-ph/0208530)
- Zdziarski, A. A., Johnson, W. N., Done, C., Smith, D., McNaron-Brown, K. 1995, *ApJ*, 438, L63
- Zdziarski, A. A., Lubiński, P., & Smith, D. A. 1999, *MNRAS*, 303, L11

TABLE 1
EXPOSURE TIMES AND COUNT RATES

Instrument	Observation Date (UT)	Exposure Time (ks)	Source Count Rate (s^{-1})	Background Count Rate (s^{-1})	Energy Range (keV)
<i>ROSAT</i> PSPC	1991 Oct. 24	9.98	0.33 ± 0.02	0.091	0.2–2.5
<i>ASCA</i> SIS 0	1999 Feb. 19	50.75	0.268 ± 0.003	0.041	0.6–8.0
<i>ASCA</i> SIS 1	1999 Feb. 19	50.66	0.171 ± 0.002	0.025	1.2–8.0
<i>ASCA</i> GIS 2	1999 Feb. 19	55.08	0.165 ± 0.002	0.014	0.9–10.0
<i>ASCA</i> GIS 3	1999 Feb. 19	55.06	0.207 ± 0.002	0.014	0.9–10.0

TABLE 2
PARAMETERS OF BEST-FITTING CONTINUUM MODELS ^a

Parameter	<i>ASCA</i>			<i>ROSAT</i>
	Simple Power Law	Broken Power Law	Power Law Plus Reflection ^b	Simple Power Law
Power Law Photon Index, Γ	1.58 ± 0.04	$1.6_{-0.6}^{+1.0}$ ^c	$1.59_{-0.07}^{+0.10}$	< 2.2
Absorbing Column, N_H (10^{21} cm ⁻²)	2.8 ± 0.3	$2.7_{-1.0}^{+1.4}$	$2.9_{-0.4}^{+0.5}$	$1.0_{-0.8}^{+4.0}$
Flux Density at 1 keV (μ Jy) ^d	1.7 ± 0.2	1.6 ± 0.1	1.7 ± 0.2	$0.8_{-0.1}^{+0.2}$
Break Energy (keV)	...	2.4 ^e
High-Energy Photon Index, Γ_2	...	$1.59_{-0.08}^{+0.03}$
Reprocessor Solid Angle, $\Omega/2\pi$	0.4	...
Reprocessor Inclination Angle, i ($^\circ$)	10	...
Power Law Cutoff Energy (keV)	100 (fixed)	...
Reduced χ^2 and d.o.f.	1.053/279	1.060/277	1.058/277	
Flux (10^{-11} erg s ⁻¹ cm ⁻²) ^{d,f}	1.2 ± 0.2	$0.13_{-0.09}^{+0.05}$
Luminosity (10^{43} erg s ⁻¹) ^{d,f}	3.1 ± 0.6	...	100	$0.3_{-0.2}^{+0.1}$
Bandpass (keV)	2–10	0.5–2.0

^a All error bars correspond to 90% confidence limits

^b Abundances of heavy elements were held fixed to their Solar values

^c The low-energy power-law index, below the break energy

^d Derived from the normalization of the spectrum. If N_E is measured in photons s⁻¹ cm⁻² keV⁻¹, then $f_\nu(1 \text{ keV}) = 663 N_E \mu\text{Jy}$. In the case of *ASCA* the uncertainty is dominated by uncertainties in the absolute sensitivities of individual instruments. In the case of *ROSAT* the normalization was determined after assuming that $\Gamma = 1.6$, with the uncertainty depending only on the uncertainty in the total number of counts

^e The break energy was constrained to lie between 1 and 4 keV based on the results of Woźniak et al. (1998).

^f Fluxes are not corrected for absorption, while luminosities are.

TABLE 3
MEASURED PROPERTIES OF UV ABSORPTION LINES

Ion and Transition	Rest EW (\AA)		FWHM _{in} ^b (km s^{-1})	Notes ^c
	Measured	Corrected ^a		
Si III $\lambda 1206$	1.1 ± 0.2	1.8 ± 0.3	430	$f_C \approx 0.6$
H I Ly α $\lambda 1216$	1.9 ± 0.4	2.4 ± 0.5	500	$f_C \approx 0.8$
Si II $\lambda 1260$	< 1.0	< 1.7	500	assumed FWHM _{in} ; assumed $f_C = 0.6$
C II $\lambda 1334$	0.9 ± 0.2	1.5 ± 0.2	290	assumed $f_C = 0.6$
Al II $\lambda 1671$	< 1.4	< 2.3	500	assumed FWHM _{in} ; assumed $f_C = 0.6$
Fe II $\lambda 2599$	3.6	Large uncertainty due to severe blending
Fe II $\lambda 2585$	2.5	Large uncertainty due to severe blending
Fe II $\lambda\lambda 2562, 2563$	4.4	Combined EW of doublet
Mg II $\lambda 2796$	3.9 ± 0.6	8 ± 1	580	$f_C \approx 0.5$
Mg II $\lambda 2803$	4.0 ± 0.7	8 ± 1	580	$f_C \approx 0.5$
Mg I $\lambda 2853$	1.8 ± 0.1	4.5 ± 0.3	400	$f_C \approx 0.4$

^a EW corrected for the effect of partial coverage, wherever applicable, as discussed in the text.

^bThe uncertainty in the FWHM_{in} is typically 50 km s^{-1}

^c f_C is the coverage fraction of the background source(s), as discussed in §6.1 of the text. For consistency with other lines, $f_C = 0.6$ is assumed in cases when it cannot be estimated. FWHM_{in} = 500 km s^{-1} was assumed in the determination of EW upper limits.

APPENDIX

THE X-RAY SPECTRUM OF MS 1718.6+4902

The galaxy MS 1718.6+4902 was detected as an X-ray source in the *Einstein* Medium Sensitivity Survey (EMSS; Maccacaro et al. 1991) and identified as an AGN at $z = 0.198$ by Stocke et al. (1991). It is close enough to Arp 102B that it fell in the field of view of both the *ROSAT* PSPC and the *ASCA* GIS and it was detected by all of these instruments with net count rates of 0.02 s^{-1} and 0.04 s^{-1} respectively. We extracted and analyzed the spectra of this object as described in §2 and §4. We find that the *ASCA* GIS spectra are well described by a heavily absorbed power law (appropriately redshifted) of photon index $1.5^{+0.2}_{-0.1}$ and column density of $(1.2 \pm 0.3) \times 10^{22} \text{ cm}^{-2}$ (the reduced χ^2 is 1.085 for 72 degrees of freedom). The observed 2–10 keV flux implied by this model is $2.8 \times 10^{-12} \text{ erg s}^{-1} \text{ cm}^{-2}$ and the intrinsic luminosity, after correcting for absorption, is $5 \times 10^{44} \text{ erg s}^{-1}$. This absorbing column must be intrinsic to the AGN since the Galactic column, inferred from the reddening reported by Schlegel et al. (1998), is only $1.4 \times 10^{20} \text{ cm}^{-2}$. The *ROSAT* spectrum, whose S/N is relatively poor, is also consistent with this model, although with a normalization that is a factor of 40% higher than that of the *ASCA* spectra, presumably due to variability of the source. In Figure A9 we show the spectra with the best-fitting model superposed, while in Figure A10 we show the 90% confidence contours in the photon index–column density plane.

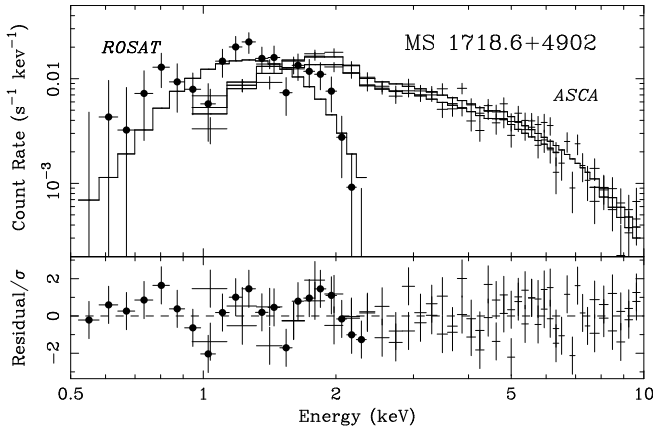


FIG. A9.— *Upper Panel*: Spectra of MS 1718.6+4902 from the *ASCA* GIS and *ROSAT* PSPC with the best-fitting model superposed. The model is an appropriately redshifted, heavily absorbed power law with parameters as given in the text. *Lower Panel*: Residuals from the subtraction of the best-fitting model from the data, scaled by the error bar at each point.

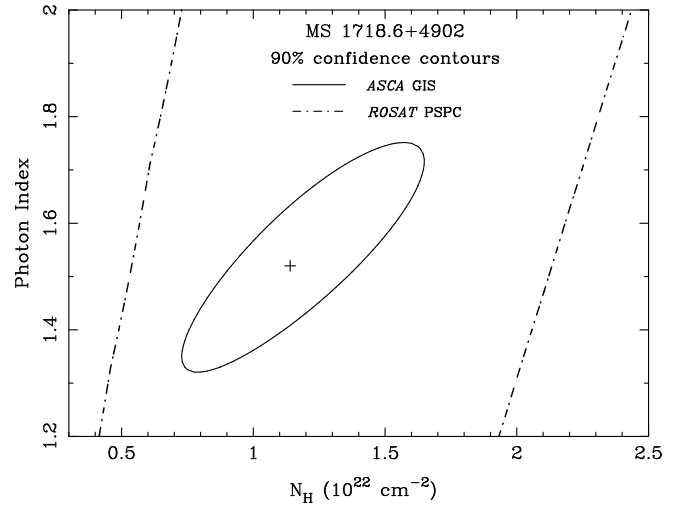


FIG. A10.— The 90% confidence contours from the power-law model fit to the spectra of MS 1718.6+4902. The solid lines shows the constraints derived from the *ASCA* GIS spectra, while the dot-dashed line shows the constraints derived from the *ROSAT* PSPC spectrum.